International Journal of Thermal Sciences 145 (2019) 106010

Contents lists available at ScienceDirect

International Journal of Thermal Sciences

journal homepage: www.elsevier.com/locate/ijts

Effect of carotid artery stenosis on neck skin tissue heat transfer

Ashish Saxena[a], E.Y.K. Ng[a,*], Mrudang Mathur[b], Chirag Manchanda[c], Nehal Amit Jajal[b]

[a] School of Mechanical and Aerospace Engineering, Nanyang Technological University, 50 Nanyang Ave, Singapore, 639798, Singapore
[b] Mechanical Engineering, Delhi Technological University, Shahbad Daulatpur, Main Bawana Road, Delhi, 110042, India
[c] Mechanical Engineering, Manipal Institute of Technology, Udupi Karkala Road, Manipal, Karnataka, 576104, India

ARTICLE INFO

Keywords:
Atherosclerosis
Carotid artery stenosis
Hemodynamics
Conjugate heat transfer
Skin temperature

ABSTRACT

The buildup of plaque in the carotid artery leads to the narrowing of the arterial lumen, known as stenosis. Arterial stenosis affects the supply of blood to the brain and may result in stroke if the plaque is dislodged. This study aims to evaluate stenosis influenced hemodynamics of the carotid artery and its effect on the bio-heat transfer to the external neck skin surface. *Systolic* and *Diastolic* carotid artery flow inlet conditions, using a finite volume numerical scheme, are simulated with the inclusion of varied stenosis degree in the carotid model (25%–90%). A 3-dimensional (3D) conjugate heat transfer study is performed on an idealized carotid artery geometry, encapsulated in a tissue model resembling the human neck. With no significant difference in the average external neck skin temperature, variation in the temperature contours is observed between stenosed and non-stenosed cases. With the increase in the carotid artery stenosis, a quantitative change, the presence of a colder region called '*cold feature*', in external neck skin temperature features is reported. This numerical study will prove to be a strong basis for future patient-specific evaluations.

1. Introduction

The carotid artery is the primary supplier of oxygenated blood to the human brain. It originates at the aortic arch and moves upwards on either side of the neck as common carotid artery (CCA), which bifurcates into the internal carotid artery (ICA) and the external carotid artery (ECA) – supplying blood to the brainstem and the face, respectively. The junction of CCA separation into ICA and ECA is known as the carotid bifurcation. Given the curved and non-uniform geometry, the velocity profile in the carotid artery can develop certain sites where wall shear stress oscillates; this initializes the localization of atherosclerotic diseases. As a result, the lumen of the artery narrows down; causing stenosis. Alerting the defense mechanism of the body, the platelets at these sites gets activated. This causes thrombosis that leads to a complete choke in the blood flow [1,2]. The occlusion of the arterial lumen starves the brain of an adequate blood supply leading to an impairment in the brain function. At times, extended periods of reduced blood supply cause permanent damage to the vascular tissue present in the brain. The deposition of stenosis tissue also poses another serious threat, that of a stroke. When this deposition in the arterial lumen is suddenly dislodged, it travels along the internal carotid artery into the brain until it enters a segment of the cerebral vasculature, too narrow for it to pass through. The stenosis tissue is, therefore, lodged in the brain causing a stroke which may lead to death [3,4]. To prevent such a situation, timely detection of atherosclerosis, by observing the arterial occlusion, also known as arterial stenosis, is one of the important milestones in the treatment profile.

Complex hemodynamics, in the presence of stenosis, can be studied using computational methods, like computational fluid dynamics, to evaluate the wall shear stress and flow separation zones [5–7]. Numerically investigating the unsteady vortical flow in the flow separation zone distal to the stenosis, Bluestein et al. [8] presented a detailed analysis on the vortex shedding in case of 84% area reduction at the throat of stenosis. Covering a wide range of Reynold (*Re*) numbers, from 300 to 1800, the authors found that the periodic shedding started at $Re = 360$ and continued thereafter for the complete range of *Re* studied. However, assuming a tube with reduction in diameter as a stenosis model, is a gross simplification of the flow domain that disregards the geometrical complexity of *in-vivo* stenotic flows. The carotid artery hemodynamics, in a relatively close to *in-vivo* geometry model, was first studied by Bharadvaj et al. [9,10], wherein using patient-specific angiography data, the authors focused on the reconstruction of a fictitious arterial bifurcation model and flow visualization within it. This has been the cornerstone of subsequent numerical studies of carotid artery hemodynamics. Following this, Perktold et al. [11] performed a numerical analysis on the effect of bifurcation angle on the

* Corresponding author.
E-mail address: mykng@ntu.edu.sg (E.Y.K. Ng).

https://doi.org/10.1016/j.ijthermalsci.2019.106010
Received 20 February 2019; Received in revised form 2 July 2019; Accepted 2 July 2019
Available online 04 July 2019
1290-0729/

Nomenclature

A	Area of cross-section (m^2)
C_{Pb}	Specific heat capacity of blood (3600 J/kg K)
C_{Pn}	Specific heat capacity of neck tissue (3600 J/kg K)
C_{Pst}	Specific heat capacity of stenosis tissue (4080 J/kg K)
D	Diameter (m)
	Natural convection heat transfer coefficient (10 W/m^2K)
k_b	Thermal conductivity of blood (0.54 W/m K)
k_{nt}	Thermal conductivity of neck tissue (0.54 W/m K)
k_{st}	Thermal conductivity of stenosis tissue (0.48 W/m K)
l_C	Characteristic length ($4A/P$, m)
N^C	Total number of defined lower temperature nodes on the external neck skin surface
N^{avg}	Total number of nodes, on the external neck skin surface, with greater than or equal to the average temperature difference with respect to 0% stenosis case
N^T	Total number of nodes on the external neck skin surface
P	Perimeter of cross-section (m)
P_g	Gauge pressure (Pa)
$q_m^{''}$	Volumetric heat generation (33 W/m^3)
Re	Reynolds number ($\frac{Ul_C}{\eta_b}$, non-dimensional)
r	radial distance from the center of the vessel ($\sqrt{x^2 + y^2}$ m)
t	Time (s)
t_p	Time period of the pulse (s)
T	Temperature at any point in the model (K)
T_∞	Ambient temperature (294 K)
T_a	Arterial temperature (310 K)
U	CCA inlet velocity (m/s)
U_S	CCA systolic inlet velocity (m/s)
U_D	CCA diastolic inlet velocity (m/s)
u	Velocity in lateral direction (m/s)
u_{axial}	Velocity in the axial direction of the flow at any area section in the carotid artery (m/s)
v	Velocity in transverse direction (m/s)
w	Velocity in streamwise direction (m/s)
x	Lateral coordinate (m)
y	Transverse coordinate (m)
y*	Distance between the outer and the dividing wall of the ICA (non-dimensional)
z	Streamwise coordinate (m)

Greek symbols

α	Thermal diffusivity of blood ($k/\rho C_p$, m^2/s)
ρ_b	Density of blood (1060 kg/m^3)
ρ_t	Density of skin tissue (1000 kg/m^3)
ρ_{st}	Density of stenosis tissue (920 kg/m^3)
μ_b	Dynamic or absolute viscosity of blood (0.003675 Pa s)
η_b	Kinematic viscosity of blood (μ_b/ρ_b, m^2/s)
ω_b	Tissue blood perfusion rate (0.4333 Kg/ms)

flow. The authors found that the axial velocity approximately doubles as the angle of bifurcation increases from 15° to 50°. The authors utilized Casson's relation to model blood as a non-Newtonian fluid. Given its validity for flow in larger arteries, subsequent numerical studies in the field modelled blood as a Newtonian fluid [12,13]. This has further paved the way for the application of computational methods to study the patient-specific carotid geometry [14–16].

The occurrence of atherosclerosis is accompanied by an acute inflammatory reaction [17,18] that leads to the presence of high temperature spots at the site of the lesion along the carotid artery [19–21]. For the given ambient conditions, it is evident that external neck skin surface temperature is the result of bio-heat transfer between the blood flow and the skin tissue [22–26]. Zhu [27] and Dennis et al. [28] numerically studied cooling of the brain, in the event of cerebral ischemia or hyperthermia, through blood flow in the carotid artery upon application of external cooling to the neck skin surface. The authors modelled the carotid artery and jugular vein blood flow as a counter flow heat exchanger system and showed that the external cooling can directly affect the brain cooling. From these studies, it can be posited that the arterial blood flow is strongly related to the outward heat transfer to the neck skin surface. Also, it is evident that the presence of the stenosis leads to a decrease in the blood flow in the carotid artery, and hence, a lower blood flow to the facial and temporal arteries [29]. Utilizing this, in the past, carotid artery stenosis has been correlated to facial [30], ocular [31], and temporal [32] thermal maps, using contact and non-contact thermographic methods. However, none of these studies investigated the effect of arterial stenosis on the heat transfer characteristics of the carotid artery and its surrounding tissue. With the occurrence of stenosis in the artery, the pulsatile blood flow leads to the generation of periodic turbulence and an upsurge in the shear stress at the neck of the stenosis [33]. It is therefore expected that the presence of stenosis will bring about changes in the heat transfer to the surrounding tissue that may be captured in the resulting temperature map over the external neck skin surface, and hence, possibly correlate to the

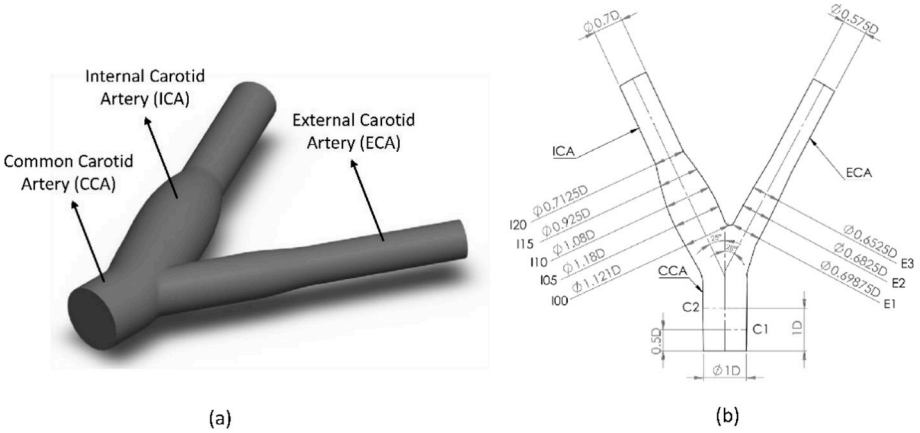

Fig. 1. Carotid artery geometry (all dimensions are in mm) (a) 3D model (b) 2D schematic (D = 8 mm). All the planes (I00 to I20 at ICA, E1 to E3 at ECA, and C1 to C2 at CCA) are respectively 5 mm away from each other.

degree of stenosis in the carotid artery.

In the literature, numerical work by Yang and Liu [34] is the only evidence of the effect of carotid stenosis on neck skin temperature contours. The authors have shown that increasing the width of the stenosis (for the same location and thickness of the stenosis tissue), from 3 mm to 8 mm, decreases the temperature on the skin surface by 0.06%, with an increase in the low-temperature region. However, the study is limited by the geometry of the carotid artery, wherein only the CCA section of the carotid artery was modelled that too as a cylinder tube. In the present study, a full carotid artery bifurcation model (including CCA, ICA, and ECA) is used to study the conjugate heat transfer between the carotid artery flow and the surrounding neck tissue. Effect of this conjugate heat transfer on the external neck skin surface temperature, with the occurrence of varying degree of stenosis in the carotid artery, is presented.

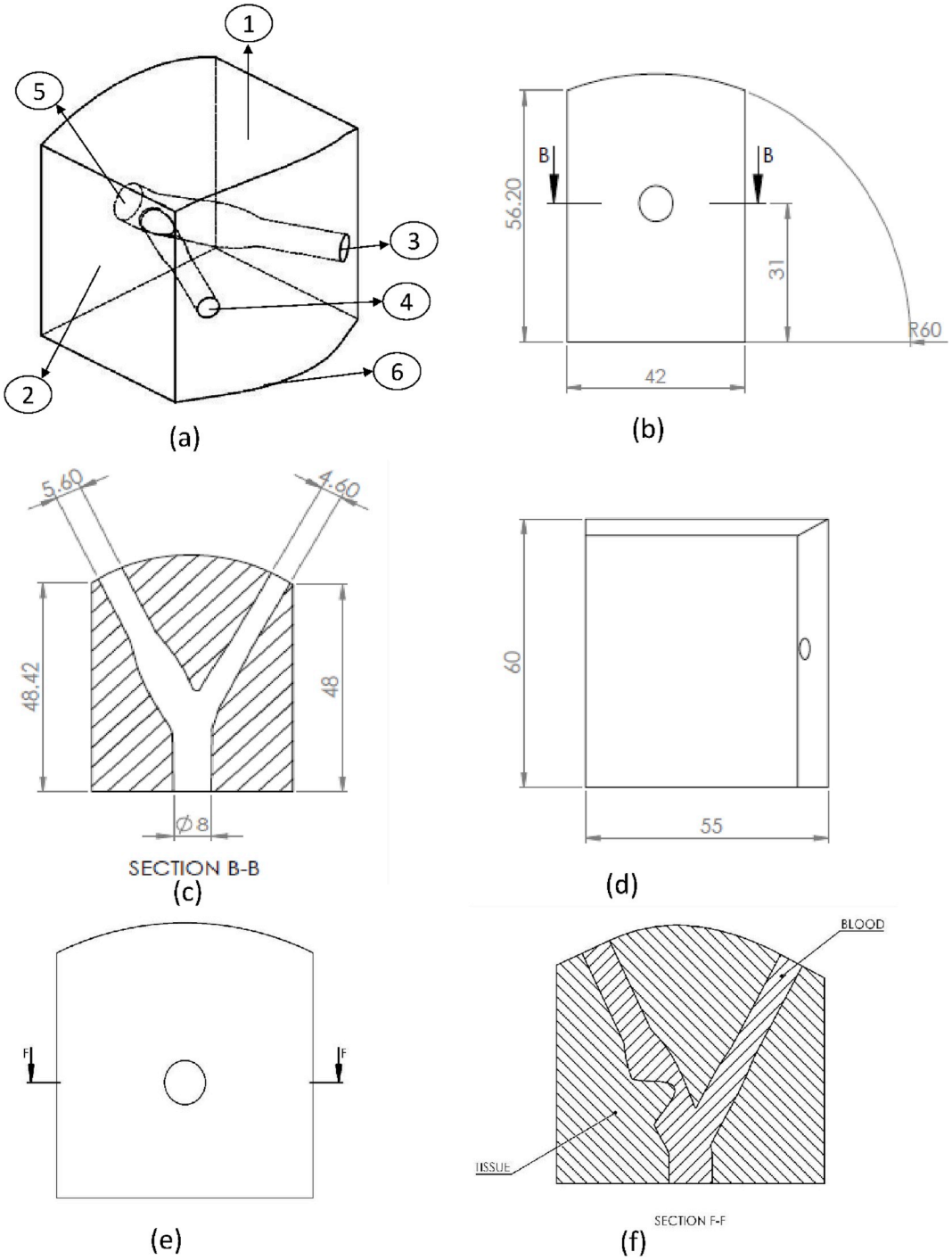

Fig. 2. (a) Schematic of geometrical zones (1–6) in 3-D encapsulated model isometric view: 1-External neck encapsulation tissue surface, 2-lateral internal neck encapsulation tissue walls, 3-ICA outlet, 4-ICA outlet, 5-CCA inlet, and 6-bottom core tissue wall (b) Front view with CCA inlet (c) Sectional view at section B-B (d) Side view (e) Section F-F on the front view with CCA inlet in 75% ICA stenosed model (f) Sectional view at section F-F with 75% ICA stenosis (all dimensions are in mm).

2. Methodology

2.1. Problem description

The carotid artery bifurcation is composed of three sub-arteries: the common carotid artery (CCA), the internal carotid artery (ICA), and the external carotid artery (ECA). Since the dimensions of the carotid artery are patient specific, for computational purposes, an idealized 3-dimensional (3D) geometry model is built. The geometrical parameters are derived from literature [9], wherein the angiographic data from 22 adults, in the age group of 22–77 years, was used. In the present study, based on the occluded diameter, the stenosis in the geometries is introduced [13]. A 75% stenosed artery geometry model is shown in Fig. 2e and f.

The diameter of the CCA is 8 mm (D) and its length is 1.75D. The length of the ICA is 4.4D and that of the ECA is 4.1D (all length measurements have been made from the apex of the bifurcation geometry). The angle between the CCA and ECA is 28° and that between the CCA and ICA is 25° [10,12] (Fig. 1b). The carotid artery hemodynamics, at steady peak *Systolic* and *Diastolic* inlet flow conditions, and its related conjugate heat transfer to the encapsulating neck tissue is studied. An idealized version of the neck was constructed using the geometrical data from existing literature [35,36] and adapted into a homogenous neck tissue encapsulation (Fig. 2a–d) over the carotid artery. Using normal carotid artery, with no stenosis (0%), as a reference, models with 25%, 40%, 75%, and 90% stenosed internal carotid artery (ICA) are studied and a quantitative comparison is carried out.

2.2. Mathematical formulation

The blood flow, in 3D, is assumed to be incompressible and Newtonian with constant material (density of 1060 kg/m^3) and thermal properties (specific heat capacity and thermal conductivity of 3600 J/Kg K and 0.54 W/m K, respectively) [37]. The neck encapsulation tissue and stenosis tissue are considered as isotropic solids. As reported in the literature [36], the density, specific heat capacity, and thermal conductivity of the encapsulated neck tissue are assumed to be 1000 kg/m^3, 3600 J/Kg K, and 0.54 W/m K, respectively. Compared to the neck encapsulation tissue, the stenosis tissue is given a lower density and thermal conductivity of 920 kg/m^3 and 0.48 W/m K, respectively, and a higher specific heat capacity of 4080 J/Kg K [18,38]. The interface between neck encapsulation tissue and artery was set as a coupled wall to enable the conjugate heat transfer formulation. In the work of Rappitsch and Perktold [39], it is shown that while the spatial characteristics remain the same, the contribution of the time-dependent oscillatory nature of the blood flow towards wall flux of albumin, a protein in blood plasma (strongly related to the wall shear stress), varies up to only 30% as compared to the steady flow solution. Taking advantage of such an observation, Ley and Kim [18] applied a steady numerical scheme solution to study the heat transfer along the stenosis tissue in the carotid artery. Additionally, Yang and Liu [34] showed the time-steady temperature distribution on the cervicum (neck) skin surface that correlates to the presence of stenosis in the carotid artery model. Such a steady conjugate heat transfer solution, as a preliminary theoretical modelling step, is justified against the computational cost. Therefore, in the present study, to simulate the problem, fluid flow and heat transfer governing steady Navier–Stokes and energy equations are solved, respectively, as expressed in the following Cartesian coordinate system:

$$\textit{Continuity}: \frac{\partial u}{\partial x} + \frac{\partial v}{\partial y} + \frac{\partial w}{\partial z} = 0 \tag{1}$$

$$\textit{Momentum in } x-\textit{direction}: u\frac{\partial u}{\partial x} + v\frac{\partial u}{\partial x} + w\frac{\partial u}{\partial x} = -\frac{1}{\rho_b}\frac{\partial p}{\partial x} + \eta\left(\frac{\partial^2 u}{\partial x^2} + \frac{\partial^2 u}{\partial y^2} + \frac{\partial^2 u}{\partial z^2}\right) \tag{2}$$

$$\textit{Momentum in } y-\textit{direction}: u\frac{\partial v}{\partial y} + v\frac{\partial v}{\partial y} + w\frac{\partial v}{\partial y} = -\frac{1}{\rho_b}\frac{\partial p}{\partial y} + \eta\left(\frac{\partial^2 v}{\partial x^2} + \frac{\partial^2 v}{\partial y^2} + \frac{\partial^2 v}{\partial z^2}\right) \tag{3}$$

$$\textit{Momentum in } z-\textit{direction}: u\frac{\partial w}{\partial z} + v\frac{\partial w}{\partial z} + w\frac{\partial w}{\partial z} = -\frac{1}{\rho_b}\frac{\partial p}{\partial z} + \eta\left(\frac{\partial^2 w}{\partial x^2} + \frac{\partial^2 w}{\partial y^2} + \frac{\partial^2 w}{\partial z^2}\right) \tag{4}$$

$$\textit{Energy}: u\frac{\partial T}{\partial x} + v\frac{\partial T}{\partial y} + w\frac{\partial T}{\partial z} = \alpha\left(\frac{\partial^2 T}{\partial x^2} + \frac{\partial^2 T}{\partial y^2} + \frac{\partial^2 T}{\partial z^2}\right) \tag{5}$$

where, $\eta = \frac{\mu}{\rho}$, $\alpha = \frac{k}{\rho C_p}$

$$k_{nt}\left(\frac{\partial^2 T}{\partial x^2} + \frac{\partial^2 T}{\partial y^2} + \frac{\partial^2 T}{\partial z^2}\right) + [(\rho_b c_{pb}\omega_b)^*(T_a - T)] + q_m^{'''} = 0 \tag{6}$$

In the neck encapsulation tissue, to simulate, tissue perfusion is considered. Tissue perfusion is the passage of blood through the circulatory system or lymphatic system (capillary bed in the tissue) to an organ or a tissue. Pennes bio-heat equation (Equation (6)), that mathematically describes the effects of tissue perfusion (ω_b) and volumetric heat generation ($q_m^{'''}$) on the bio-heat transfer, is used [40].

2.3. Boundary conditions

Referring to the geometrical zones (1–6), in Fig. 2a, the following

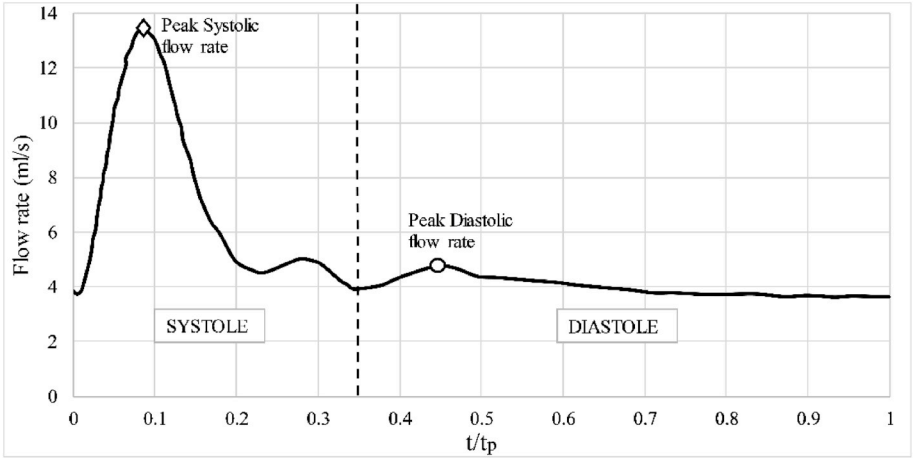

Fig. 3. Physiological flow-rate curve (***t*** = time in s and = time period of the pulse in s) [11].

boundary conditions are applied to the 3D neck tissue encapsulated carotid artery model:

Zone-1 (external neck skin surface): $T_\infty = 294K$, $h_{NC} = 10\ \mathrm{W}m^{-2}K^{-1}(natural\ convection)$[41];

Zone-2 (lateral internal neck tissue walls): $\frac{\partial T}{\partial n} = 0\ (adiabatic)$ [34];

Zone-3 and 4 (ICA and ECA outlet): $P_g = 0$Pa (Pressure outlet) [42];

Zone-5 (CCA velocity inlet): $w = U^*\left(1 - \frac{r^2}{(D/2)^2}\right)$ (*fully developed parabolic inlet*), u= $v = 0$, $T = 310\ K$ [18,34];

Zone-6 (bottom core neck tissue wall): $T = 310\ K$ (*isothermal*) [34].

In the diagnosis of carotid stenosis, hemodynamics at the peak systolic and diastolic velocities are of great interest to clinicians and researchers [42,43]. Therefore, in the present study, peak *Systolic* and *Diastolic* flow rates (Fig. 3) were extracted from the physiological flow-rate curve utilized by Perktold et al. [11] and applied to the *Systolic* ($U_S = 0.5332\ m/s$) and *Diastolic* ($U_D = 0.1908\ m/s$) velocity inlet flow condition simulations, respectively.

2.4. Numerical procedure

The finite volume method has been employed to obtain the numerical solution of the governing equations. This has been implemented through the commercially available computational fluid dynamics software FLUENT (version 19.1) by ANSYS Inc. Pressure-velocity coupling is achieved through the Semi Implicit Pressure Linked Equations (SIMPLE) algorithm [44] and a second-order upwind scheme has been utilized for the spatial discretization of momentum and energy transport equations. Green-Gauss Cell based gradient reconstruction scheme has been used with weighted residuals convergence criteria of 10^{-10} for each of the continuity, velocity components in x, y and z direction, and energy equations. A laminar viscous model is employed with energy and momentum relaxation factors set to 0.7 and 0.5, respectively. All the simulations are found to be converged within the set maximum number of iterations (100,000). On 12-compute threads of an Intel(R) Xenon(R) CPU E5-1650 v4 3.60 GH computer, an average wall-clock time per iteration is found to be 1.567 s for a typical mesh size of 5×10^6 number of cells.

2.5. Mesh-independent study and validation of results

To determine the accuracy of the created idealized carotid artery bifurcation geometry (0% stenosis), steady-state simulations are performed under the same steady conditions as used by Gijsen et al. [12] at $Re = 270$, $\mu = 2.9 \times 10^{-3}\ Pa.s$, and $\rho = 1410$ Kg/m^3. To determine the ideal mesh density for the described simulations in Section 2.1, using the same heat transfer boundary conditions as described in Section 2.3, flow and heat transfer simulations are carried out on nine different meshes, with cell number in the range of 0.15×10^6 to 12.34×10^6. For meshing, tetrahedral and prismatic type of cell elements are used. In the carotid artery wall section, an inflation layer of 1 mm is given, which is mainly comprised of prismatic elements. Similarly, at the external neck skin surface and bottom body core wall, an inflation layer of 2 mm is used. The rest of the model volume is dominated by tetrahedral type of elements. The area average temperature on the external neck skin surface and average velocity at plane I00 (Fig. 1b) are plotted against the number of cells (Fig. 4).

For velocity calculation, the percentage error between mesh 6 and 7, 7 and 8, and 8 and 9, is found to be 0.77%, 0.72%, and 0.04%, respectively, while for temperature, the error is found to be less than 0.0003% for any two-consecutive meshes, from mesh 6 to 8. Given the error percentage is less than 1% for mesh 6 and 7, a mesh size of 5×10^6 (mesh 6) is finally used for reporting the resultant outcome of the simulations performed. For mesh 6, an average mesh skewness, aspect ratio, and orthogonality are found to be 0.20 ± 0.11, 1.97 ± 0.78, and 0.80 ± 0.11, respectively. For the model with the introduction of varied stenosis degree, in the range of 25%–90%, a similar mesh density is used. Furthermore, at 5 different planes in ICA, viz. I00, I05, I10, I15, and I20 (Fig. 1b), axial velocity profiles are compared with the previously reported numerical and experimental studies in the literature. The distance between successive planes is D/2. The axial velocity, at these planes, is normalized with the inlet CCA velocity (u_{axial}/U) and plotted against the non-dimensional distance (y*) between the outer and the dividing wall of the ICA as shown in Fig. 5. A strong agreement between the compared velocity profiles can be observed, along with a marginal variation at planes I00 and I20, which can be attributed to the slight variations in the geometric parameters, viz. curved plane smoothing, fillet radius at the bifurcation junction, etc., used for the 3D reconstruction, among the studies used for the comparison.

3. Results and discussion

In this section, results pertaining to the change in carotid artery hemodynamics and heat transfer (at *Systolic* and *Diastolic* inlet velocity flow conditions), in the presence of varied stenosis degree (from 25% to 90%) in the ICA, are presented. First, the flow streamlines, velocity profiles, pressure drop, and flow division in the ICA are used to understand the carotid artery hemodynamics, then, its effect on the resultant thermal features, at the external neck skin surface, are qualitatively and quantitatively studied.

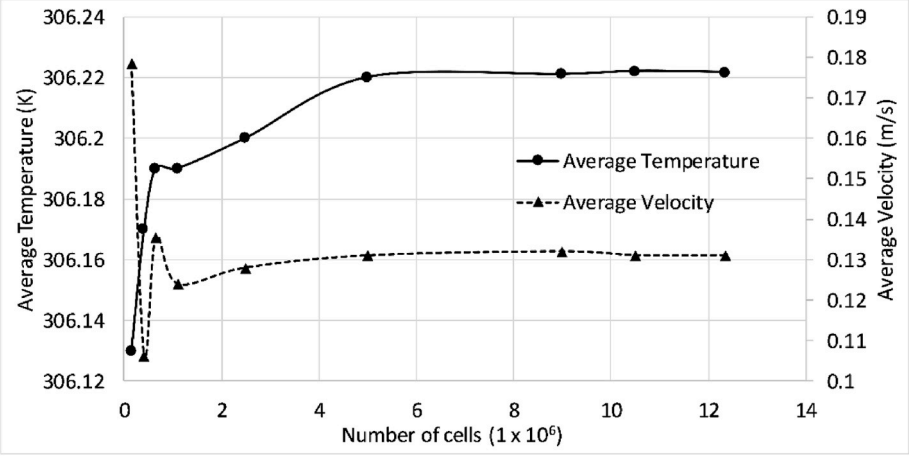

Fig. 4. Grid independency plot for average temperature on the external neck skin surface and average velocity at plane I00.

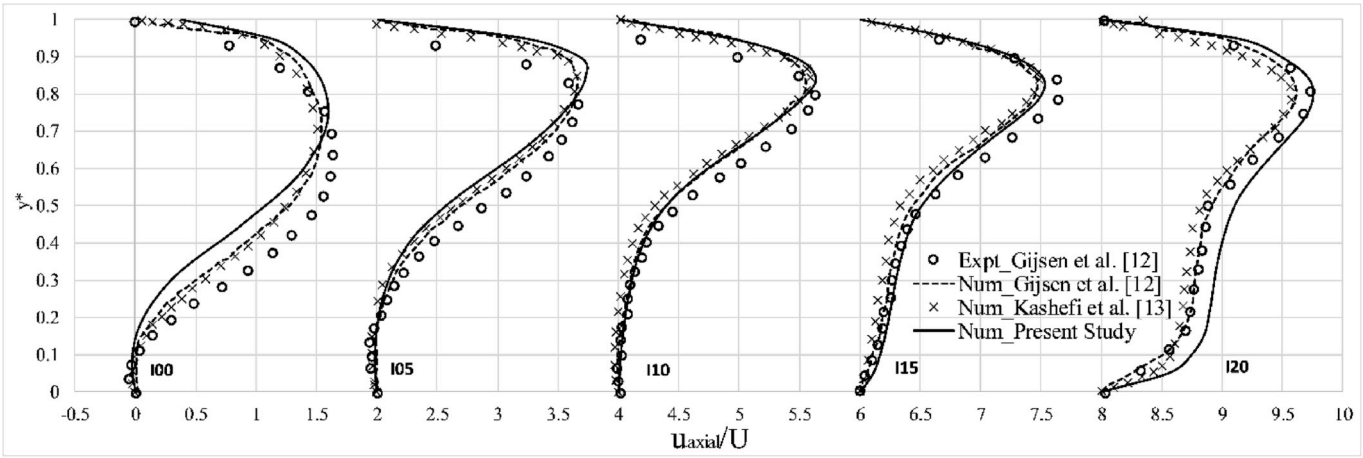

Fig. 5. Validation of results (axial velocity profile in ICA) with previous experimental and numerical work on 0% stenosis blood flow in carotid bifurcation geometric model (u_{axial}/U displaced by a factor of 2 for representation purpose).

3.1. Carotid artery flow

For the normal case (0% stenosis), of the total flow in the CCA, the division of flow is found to be 35:65 and 36:64 between ECA and ICA, for *Diastolic* and *Systolic* inlet flow conditions, respectively (Table 1). The streamlines in both *Systolic* and *Diastolic* phase (Fig. 6) show a minute stagnation in the flow near the non-dividing wall of the ICA lumen, while the flow is undisturbed in other parts of the artery. This stagnation of flow is mainly because of the sudden enlargement in the geometry (lumen bulb) for the given flow conditions. Given the inlet velocity condition in *Systolic* flow is higher than *Diastolic* flow (2.8 times), the flow stagnation is expected to be higher in case of *Diastolic* flow (Fig. 6). This is evident from the fact that even with a higher pressure drop in the ICA region (from I00 to I20) of *Systolic* flow (45 Pa as compared to 9 Pa in Table 1), the actual pressure value at I20 is found to be almost four times higher than *Diastolic* flow (53 Pa versus 13.50 Pa). In Fig. 7a and b, it can be observed that from upstream to midstream planes (I00 to I10), the flow remains stagnant ($u_{axial}/U_s = 0$) for 30%–50% of the distance (y*) from non-dividing to dividing ICA wall. As the flow reaches the downstream planes (I15 and I20), the lumen diameter gradually decreases and hence, the flow stagnation disappears. Interestingly, for both *Systolic* and *Diastolic* flow cases, from upstream to downstream planes, the point of maximum axial velocity (in the range of 1.5–2 times of U_s) gradually shifts towards the dividing wall of ICA.

As the stenosis appears in the ICA lumen bulb, the flow and heat transfer are similar to the case of flow past an obstruction (bluff body) [45–47]. It can be observed in Fig. 6, for stenosis up to 40%, the streamlines show the formation of recirculation zone before the stenosis, while above 40% (Fig. 6), the downstream flow becomes highly chaotic with the formation of recirculation zones on the either sides of the stenosis. Moreover, from Fig. 7a and b, the flow velocity disturbances are found to be more pronounced in *Systolic* flow case (25%–90% stenosis), along with backflow velocity profile in the downstream (I15 and I20) for stenosis over 40% in both *Systolic* and *Diastolic* flow cases. This can be further corroborated from the fact that as the stenosis goes above 40%, pressure drop in the ICA (across the stenosis, P_{I20}-P_{I00}) is found to have increased up to 10 times. This is mainly because of the huge obstruction in the flow that changes the flow division between ICA and ECA.

For both *Systolic* and *Diastolic* inlet flow conditions, as the stenosis increases to 75%, the flow in ICA changes from around 64% of the inlet flow condition to around 50%, which has further decreased to around 20% as the stenosis increases to 90% (Table 1). For stenosis up to 40%, the maximum velocity around the neck of the stenosis (I10), in case of *Systolic* and *Diastolic* flows, is found to be around 0.5 and 2.7 times of the inlet velocity (U_s), respectively. As the stenosis goes above 40%, this maximum velocity, for *Systolic* and *Diastolic* flow cases, goes up to 1.33 and 3.33 times of U_s, respectively. This will bring distinction in the heat transfer characteristics, which is discussed in the next section.

3.2. Heat transfer analysis

In this study, the thermal interaction between three domains: blood, skin tissue, and the external ambient environment, has been investigated using conjugate heat transfer formulation. It is evident that the convective heat transfer due to blood flow in the carotid artery will lead to the development of a temperature profile at the carotid artery wall and the neck tissue interface. Following this, along with the blood perfusion and volumetric heat generation, thermal diffusion will take place in the neck tissue encapsulation. This diffused heat will finally interact with the external neck skin surface. Given that the external neck skin surface is applied with ambient natural convective boundary condition (Section 2.3), a resultant temperature profile at the external

Table 1
Pressure drop and flow division summary for different stenosis cases studied.

% Stenosis	Pressure Drop (Pa)						% Flow Division			
	Systolic flow			Diastolic flow			Systolic flow		Diastolic flow	
	CCA (P_{C2}-P_{C1})	ECA (P_{E3}-P_{E1})	ICA (P_{I20}-P_{I00})	CCA (P_{C2}-P_{C1})	ECA (P_{E3}-P_{E1})	ICA (P_{I20}-P_{I00})	ECA	ICA	ECA	ICA
0	0.19	13.90	45.66	0.40	3.47	9.00	36.45	63.55	34.78	65.22
25	0.19	14.18	45.39	0.41	3.51	9.07	36.44	63.56	34.84	65.16
40	0.20	14.23	46.31	0.40	3.55	9.57	36.54	63.46	35.10	64.90
75	0.16	27.23	210.66	0.40	5.93	35.85	49.14	50.86	47.81	52.19
90	0.25	69.22	497.59	0.40	13.73	92.10	81.31	18.69	80.55	19.45

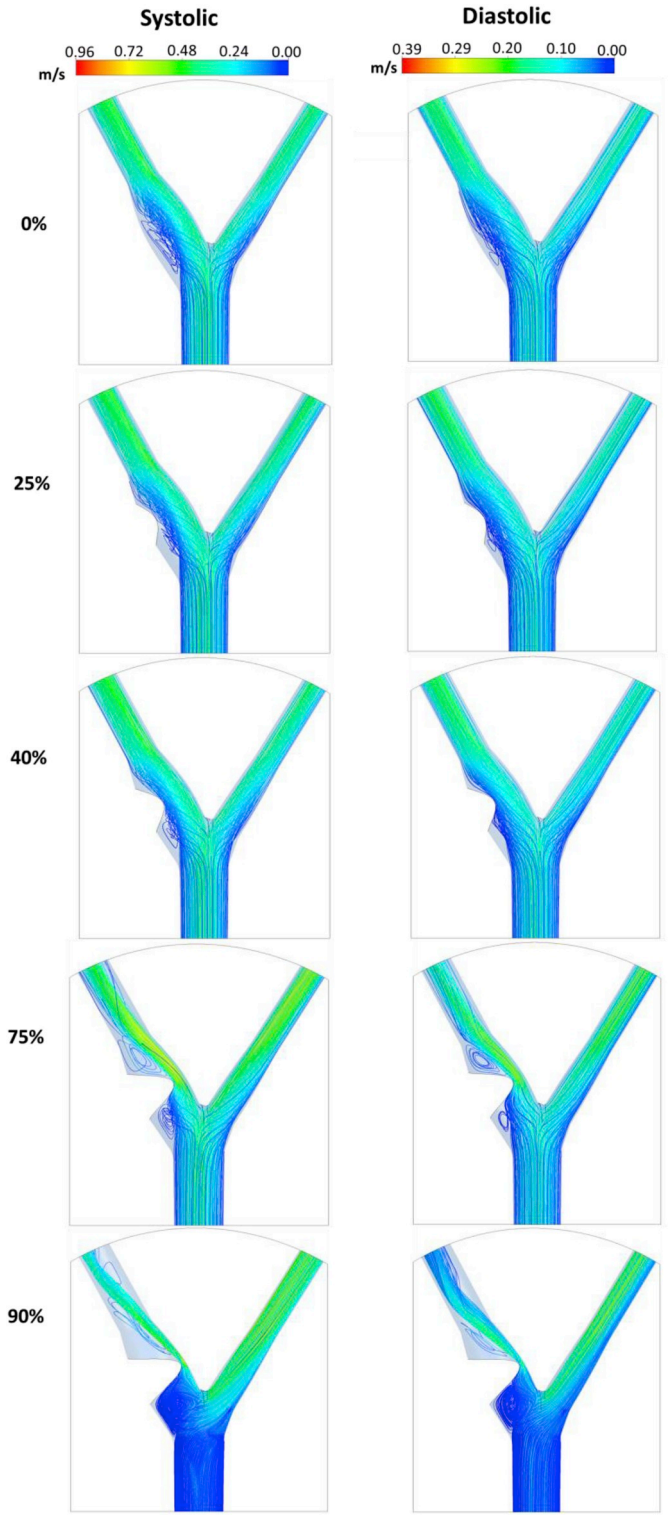

Fig. 6. Velocity streamlines for different stenosis at Systolic and Diastolic inlet flow conditions.

neck skin surface will occur.

In the 3D geometry model, from the sectional view B–B (Fig. 2c), the ICA, with a larger diameter as compared to the ECA, has a higher surface area to exchange heat with the surrounding neck tissue; this in return leads to a higher heat transfer on the left side as compared to the right. This is corroborated by the temperature contours at the *xz*-mid-plane (Fig. 8). Furthermore, the occurrence of flow stagnation (re-circulation zones in Fig. 6), in the lumen area, results in lower temperature regions within the ICA, which increases with the increase in the degree of stenosis (Fig. 8). As shown in Fig. 9, the temperature contours on the left side of the external skin surface show a higher temperature which directly correlates to the higher heat transfer in the region. For 0% stenosis case, with a 2.8 times higher flow rate as compared to the *Diastolic* inlet flow condition, the temperature contours under the *Systolic* inlet flow condition differs qualitatively: more elongated for Diastolic case. Though the average surface temperature is same in both the cases (Table 2), lower temperature contour, in the center region, is found to be wider. Moreover, the occurrence of a thin and elongated (in *z*-direction) jet like cold region at the bottom (referred as '*cold feature*' from here onwards) is also observed. This *cold feature* is not observed in the 0% *Systolic* case (Fig. 9). With the change in flow rate between the *Systolic* and *Diastolic* flow cases, this local change in the temperature contour is believed to be the basis for estimation of health vitals like pulse rate from the neck region temperature measurement [48,49]. The transient change in flow rate during the diastolic phase, in the pulsatile cardiac blood flow cycle (Fig. 3), results in local low temperature regions in the carotid artery flow (Fig. 8), which leads to a lower convective temperature profile on the carotid artery wall. Locally, this affects the conduction and perfusion terms in Equation (6) that alters the heat diffusion in the neck encapsulation tissue, resulting in the occurrence of a *cold feature* at the external neck skin surface. In the present study, given the *Systolic* and *Diastolic* flow conditions are simulated separately using a steady numerical scheme, the occurrence of the *cold feature* is prominently visible. In an *in-vivo* transient temperature monitoring study, this change in the local region temperature is expected to be quite small and full of noise. Hence, application of signal processing techniques, like multiresolution signal extraction method, to recover the original pulse information temperature signal [50]. Given the signal extraction is difficult from the deeply located arteries, a more superficial artery location is the best fit for such measurements [51]. In a transient numerical model with full pulsatile cardiac blood flow cycle, unlike the use of a constant perfusion value ($\omega_b = 0.4333$ Kg/ms) in the present study, a temperature dependent perfusion model may further result in an appropriate thermal perturbation at the external neck skin surface [52].

As discussed in Section 3.1, with the introduction of stenosis in the ICA, the flow streamlines, flow division, and other flow parameters are found to be affected, along with the formation of recirculation zones on either side of the stenosis. With these changes in the flow, the convective heat transfer from the carotid artery blood flow to the surrounding neck tissue will also change (Fig. 8), hence, the same will be reflected in the temperature at the external neck skin surface. Additionally, in the presence of the stenosis tissue, the temperature difference between the internal wall of the stenosis tissue (in contact with blood flow) and the outer wall (in contact with the encapsulation tissue) will be higher than any other region on the artery wall with no stenosis tissue. This will further contribute to the local lower temperature region on the external neck skin surface.

Interestingly, the average external neck skin surface temperature (Table 2) is found to be same for all the cases studied. Moreover, using a significance level of 0.05 for statistical student *t*-test, the difference in temperature values, over the external neck skin surface, between the stenosis cases (25%–90%) the 0% stenosis case, for both *Systolic* and *Diastolic* flow cases, is not found to be significant in most of the cases (Table 2). Hence, average temperature is not a good criterion to perform a comparative analysis. However, the distribution of the temperature values on the external neck surface could bring a contrast among the cases studied.

As observed in Fig. 9, the *cold feature* becomes more pronounced between *Systolic* and *Diastolic* flow cases, with a distinction in shape and size, as the stenosis increases. With the increase in stenosis, elongation in the size of the *cold feature* can be seen, which is more prominent in *Diastolic* cases. Using the length of this feature (in z-direction), a quantitative comparison can be done (Table 2). For *Systolic* flow case,

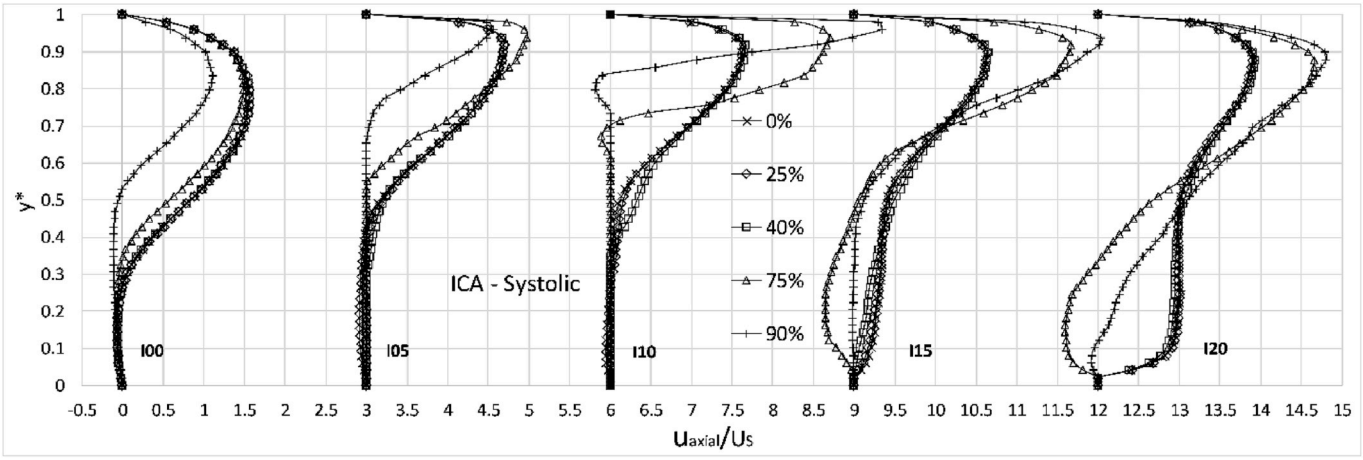

a

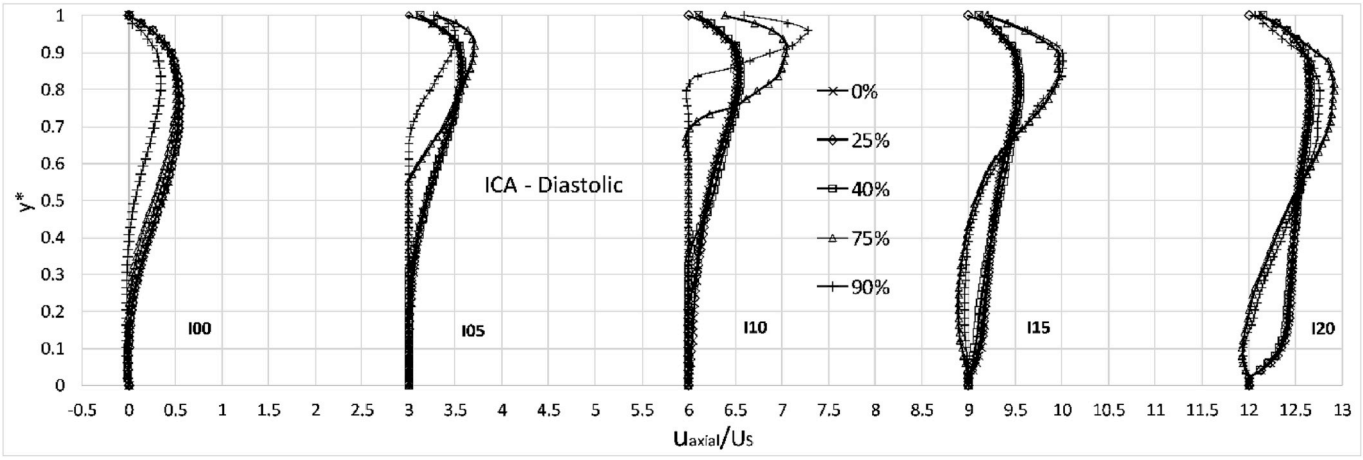

b

Fig. 7. a: Velocity profile at various sections along the ICA in Systolic flow case (u_{axial}/U_s is displaced by a factor of 3 for representation purpose) for various stenosis degree. b: Velocity profile at various sections along the ICA in Diastolic flow case (u_{axial}/U_s is displaced by a factor of 3 for representation purpose) for various stenosis degree.

with an increment of 15% from 25% to 40% stenosis, the increment in the length of the *cold feature* is also around 15%, while for *Diastolic* case, this increment is found to be as much as 84%. On the other extreme, as the stenosis reaches 90% with an increment of 15% from 75%, the *cold feature* length increases by 43% and 2%, for *Systolic* and *Diastolic* flow cases, respectively. In the latter case, the increase in the width of the cold feature is accompanied by only a minute increment in its length (Fig. 9). Also, it should be noted that the *cold feature* length in the 75% and 90% stenosis *Diastolic* cases is almost same as the length of the geometry in z-direction, which is distinct from all other cases studied. The increase in length of the cold feature with the increase in stenosis implies the decrease in heat transfer from the stenosed ICA to the surrounding tissue. This leads to the cooling of the external neck skin surface. As this effect is further enhanced with a decrease in blood flow velocity (i.e. decrease in forced convection heat transfer coefficient), as in the case of *Diastolic* flow, a comparatively higher cooling or *cold feature* length is observed.

Given the ideal nature of the geometric model used in the present numerical study, it should be noted that the presence of a *cold feature* in exact shape and size may not likely be observed in the real-time in-vivo neck skin temperature map. With an inconsistent shape, size, orientation, flow condition, depth, surrounding vasculature, etc., the actual carotid artery and neck geometry is highly complex, non-planar, and patient-specific in nature [35]. With the occurrence of stenosis *in-vivo*, however, a *cold feature* is expected to occur. As an evidence, in the past, a cholesterol ester coated flexible plate was used by Hofferberth et al. [32] to measure the forehead temperature in 300 patients and a change in the color of the plate was correlated to the presence of stenosis. Given the carotid artery is responsible for supplying blood to the temporal region of the face, the occurrence of stenosis in the carotid artery leads to a lower temperature on the same side of the temporal region. To quantify such a *cold feature* observation, a ratio of the number of comparatively lower temperature nodes (N^C) with respect to the total number of nodes (N^T), on the external neck skin surface, can be defined.

In the present study, using the maximum value of the minimum temperature occurring in all the cases as a threshold temperature ($T^C = 306.08$ K), the number of nodes with temperature less than or equal to T^C are used for the calculation of ratio N^C/N^T. Fig. 10 shows that the value of N^C/N^T increases with the increase in the stenosis in the ICA. For a specific degree of stenosis (including 0% stenosis), the value of N^C/N^T is always higher for the *Diastolic* flow case, which signifies the occurrence of colder regions as compared to the *Systolic* flow case. For both *Systolic* and *Diastolic* flow cases, although the distinction between any two consecutive stenosis cases is quite small (minimum of 4% in *Diastolic* flow case), the distinction between 0% stenosis and any stenosis is minimum of 43% (*Diastolic* flow case) and a maximum of 417% (*Systolic* flow case).

Thus far, it is established that the external neck skin surface

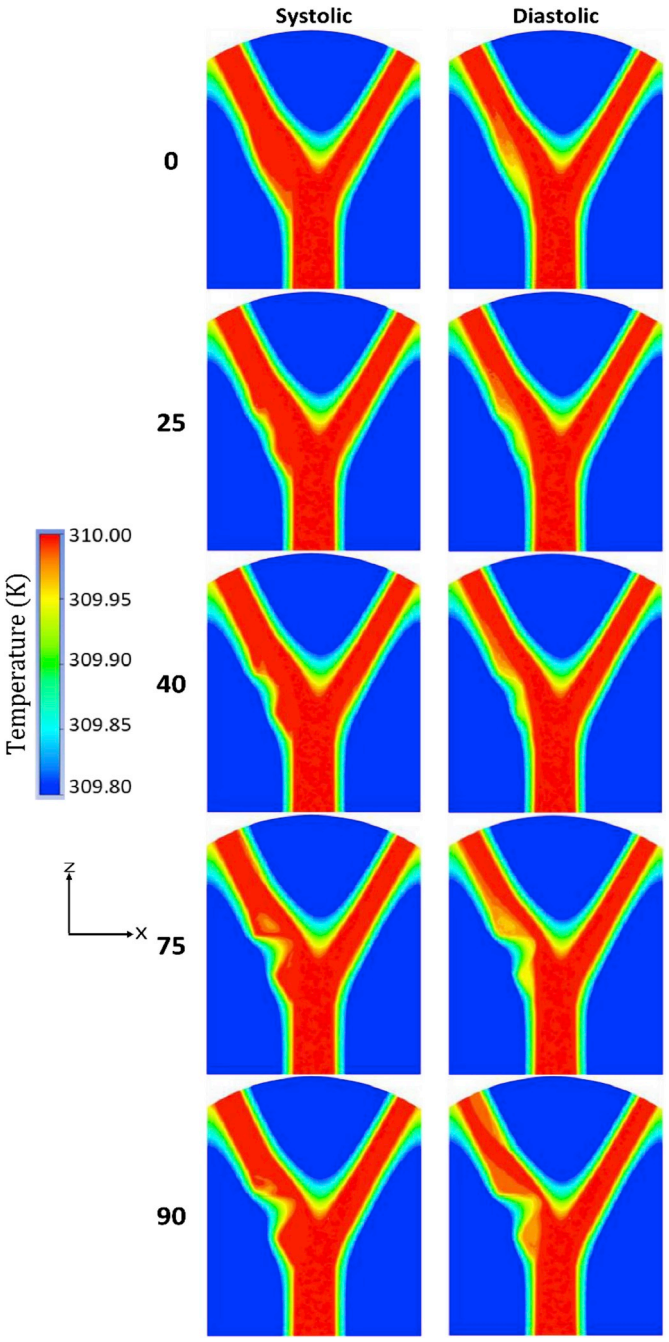

Fig. 8. Temperature contours on the xz-midplane (sectional view B–B) for different stenosis at Systolic and Diastolic flow conditions.

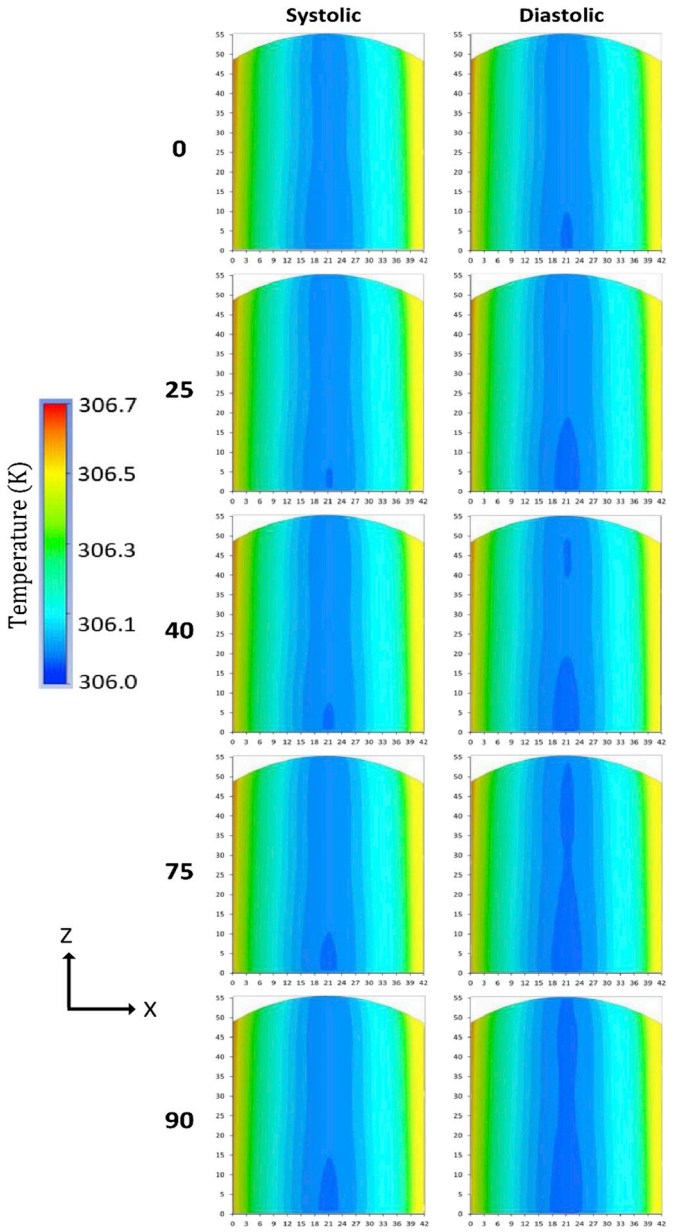

Fig. 9. Temperature contours on the external neck skin surface for different stenosis at Systolic and Diastolic flow conditions (all dimensions are in mm).

temperature contour with 0% stenosis can be easily distinguished from the stenosis case, under both *Systolic* and *Diastolic* inlet flow conditions. Using it as the reference, a subtraction-based contour enhancement can be performed for the respective 25%–90% stenosis surface temperature contours. The resultant maximum and average temperature difference values are summarized in Table 3 and the contours in Fig. 11. It is evident that a higher degree of stenosis results in a larger temperature difference. For the same stenosis, *Systolic* and *Diastolic* flow cases have a similar maximum temperature difference, however, the value increases with the increase in the stenosis in both the cases. On the other hand, except between the 25% and 90% stenosis cases, the average temperature difference shows an overlap in the standard deviation values among the cases studied (Table 3). However, the resultant contours in Fig. 11 (distribution of the nodal values) show a clear distinction among the cases studied.

It should be noted that the higher temperature difference contours are mostly occurring on the left side of the external neck skin surface, which is explained earlier; as result of location of ICA, with stenosis, on the left side, leading to the occurrence of lower temperature regions in the blood flow and the artery wall (Fig. 8). Qualitatively, the intensity and area covered by the high temperature difference contours are observed to be increasing with the increase in the stenosis degree from 25% to 90%. Moreover, given the reduced flow rate (2.8 times lower), this increase is greater in the case of *Diastolic* flow as compared to *Systolic* flow. Quantitatively, a ratio of number of nodes, on the external neck skin surface, with temperature difference value greater than or equal to the average of all the cases (N^{avg}) with respect to the total number of nodes (N^{T}) is defined. The value of N^{avg} is found to be 0.006. Using this value, the ratio (N^{avg}/N^{T}) is calculated and summarized in Table 3, which defines a parameter to distinguish different degrees of stenosis (25%–90%) from 0% stenosis. As was observed qualitatively in Fig. 11, it is evident from the value of N^{avg}/N^{T} (Table 3) that the area

Table 2
External neck skin temperature contour characteristics.

% Stenosis	Average temperature ± SD (K)		*p*-value with respect to 0% stenosis case (*t*-test)		Center *cold feature* length in z-direction (mm)	
	Systolic flow	Diastolic flow	Systolic flow	Diastolic flow	Systolic flow	Diastolic flow
0	306.22 ± 0.14	306.21 ± 0.14	–	–	0	10
25	306.22 ± 0.15	306.21 ± 0.15	0.01	0.02	6.5	19
40	306.22 ± 0.15	306.21 ± 0.15	0.02	0.03	7.5	35
75	306.21 ± 0.15	306.21 ± 0.15	0.01	0.21	10.5	54
90	306.21 ± 0.15	306.20 ± 0.15	0.32	0.50	15	55

covered by high-temperature difference contours is higher in case of *Diastolic* flow, for a specific stenosis degree. Also, with the increase in stenosis, this ratio also increases, and the increase is higher in case of *Diastolic* flow.

From a practical application point of view, a non-contact measurement (using an IR thermal camera) of such a small temperature resolution (in the third decimal place) is highly unlikely. For instance, the most thermally sensitive commercially available IR thermal camera, FLIR T1020 by FLIR Systems, Inc., provides a thermal resolution of $<0.02\,^{\circ}C$ [53], hence, any temperature value in three decimal places can't be resolved. However, resolved up to two decimal places, application of such a contour subtraction-based method is still expected to provide a quantitative difference in the area covered by the region of high temperature difference. For instance, in the work of Morgan et al. [31], thermography-measured average ocular temperature difference (between left and right ocular surfaces) was correlated (correlation coefficient, $r = -0.67$) to the difference in the degree of stenosis in the two carotid arteries (left and right) of the same patient. For a patient with 20% and 90% stenosis on the left and right carotid artery, respectively, the difference in average ocular temperature was found to be 0.74 °C. It is expected that in an *in-vivo* thermography measurement, the use of the proposed N^{avg}/N^{T} ratio, evaluated from the thermal image subtraction of the left and right ocular surface, could further strengthen the correlation coefficient.

4. Limitations

The present computational study is performed on a fictitious idealized carotid geometry. This limits its applicability to a real-time patients-specific analysis, wherein the shape, size, orientation, flow condition, and depth of artery are inconsistent [54]. However, as a preliminary study, the presented results play an important role in performing a patient-specific study in future. Given the inclusion of conjugate heat transfer, the present study is limited to only peak *Systolic* and *Diastolic* inlet flow conditions, under a steady state analysis as motivated from the past work in the field [18,55,56]. Another limitation of the present study is the rheological assumption of Newtonian blood flow. In the work of Bit and Chattopadhyay [57] ($Re = 690$) and Razavi et al. [58] ($Re = 278$), it was observed that compared to the non-Newtonian models, the use of a Newtonian model, in an approximately 60% stenosed artery geometry, overestimates the flow recirculation length across the stenosis. In an individual stenosed carotid artery geometry (25%–90% stenosis), this error in the flow recirculation length estimation will result in an error in convective heat transfer to the carotid artery wall, however, the relative change among the models (with respect to 0% stenosis case) will remain the same. Using an appropriate non-Newtonian model, the error in heat transfer estimation could be evaluated in the future study. It is evident that performing a transient conjugate heat transfer study, on a 3D numerical model with 5×10^6 number of cells while applying a pulsatile physiological inlet flow condition [59], is both computationally expensive and time intensive. Moreover, following the robust mesh independent study, the applied steady-state numerical model, in the present study, shows a good agreement with the benchmark experimental and numerical work on the modelled carotid artery geometry flow [12,13]. Therefore, for the presented results, such a trade-off offsets the limitations of the study.

5. Conclusions

In the present study, a finite-volume based computational method is used to analyze the conjugate heat transfer associated with blood flow in the carotid artery encapsulated by neck tissue. Using the geometric parameters from existing literature, an idealized 3D carotid artery

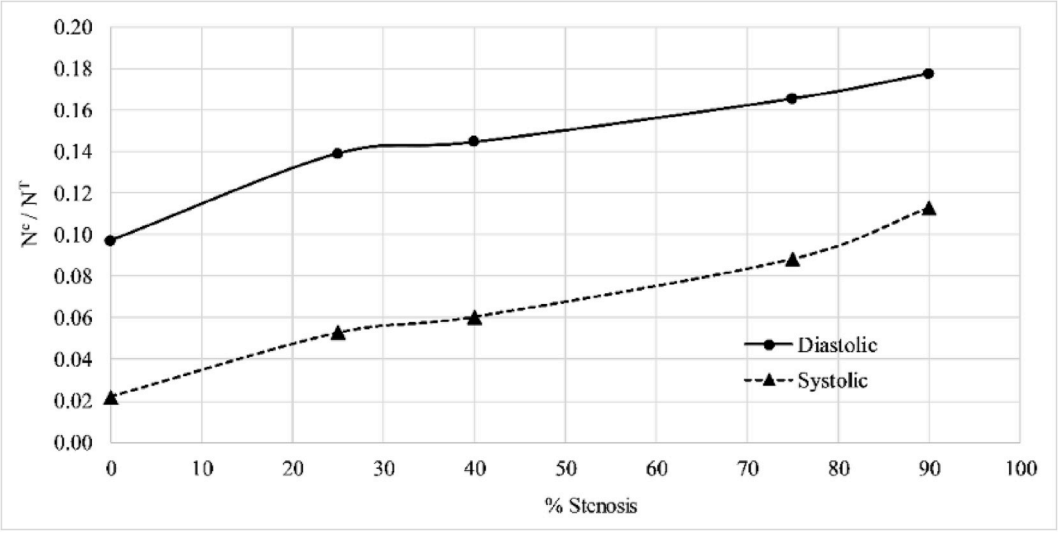

Fig. 10. External neck skin cold region nodes (N^C) with respect to total number of nodes (N^T).

Table 3
Characteristics of external neck temperature contours on subtraction with 0% stenosis case.

% Stenosis	Maximum temperature difference (K)		Average temperature difference ± SD (K)		N^{avg}/N^{T}	
	Systolic flow	Diastolic flow	Systolic flow	Diastolic flow	Systolic flow	Diastolic flow
25	0.013	0.013	0.004 ± 0.001	0.004 ± 0.001	0.01	0.02
40	0.014	0.015	0.004 ± 0.001	0.005 ± 0.001	0.08	0.14
75	0.017	0.019	0.006 ± 0.002	0.007 ± 0.002	0.46	0.66
90	0.020	0.021	0.008 ± 0.003	0.009 ± 0.003	0.76	0.85

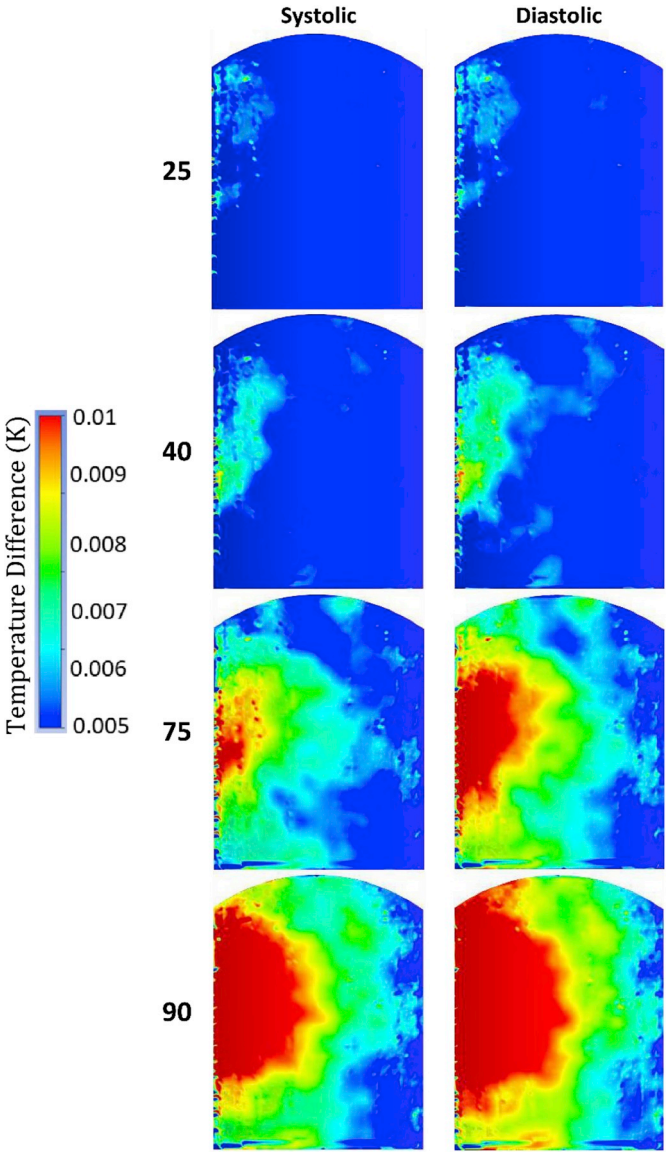

Fig. 11. Temperature difference contours on the external neck skin surface with respect to 0% stenosis case at Systolic and Diastolic flow conditions.

geometry is reconstructed and the blood flow with heat transfer is studied at two different inlet flow velocity conditions, viz. peak *Systolic* and *Diastolic* flow. For both the inlet flow conditions, carotid artery geometrical changes in terms of inclusion of varied degree of stenosis (25%–90%) in ICA are introduced. With the inclusion of stenosis, the changes in hemodynamics, viz. velocity profiles, pressure drop, flow division, and streamlines, and associated heat transfer to the external neck surface, viz. temperature contours are reported. With no distinction in the average temperature on the external neck skin surface, the introduction of stenosis shows the occurrence of a *cold feature* in the temperature contour, of which the length increases with an increase in stenosis degree. Owing to the lower velocity and hence a lower convective heat transfer, this *cold feature* is found to be more prominent in case of *Diastolic* flow. Furthermore, using a threshold lower temperature (T^C), a ratio (N^C/N^T) is defined, which signifies the extent of cooling on the external neck skin surface. With the increase in stenosis, this ratio is found to have increased, along with a minimum difference of 40% between 0% and any degree of stenosis. Lastly, taking the external neck skin surface temperature contour for 0% stenosis as a reference, a subtraction-based manipulation is performed for the varied stenosis cases. A ratio (N^{avg}/N^T), which shows that the area just over the ICA location has the maximum effect due to stenosis, is calculated. This area of influence increases with the increase in stenosis and found to be up to 85% affected in case of 90% stenosis under *Diastolic* flow. The results presented, in this preliminary study, will prove to be a benchmark for future patient-specific studies in evaluating a skin temperature map-based carotid artery stenosis detection tool.

Conflicts of interest

The authors declare that they have no conflict of interest.

Acknowledgements

The authors would like to acknowledge the SingHealth-NTU collaborative research grant (Grant number: SHS-NTU/014/2016) for the funding support to carry out this project. The authors would also like to acknowledge the NTU-India Connect program that availed the authors to collaborate and complete the study.

Appendix A. Supplementary data

Supplementary data to this article can be found online at https://doi.org/10.1016/j.ijthermalsci.2019.106010.

References

[1] S.A. Ahmed, D.P. Giddens, Flow disturbance measurements through a constricted tube at moderate Reynolds numbers, J. Biomech. 16 (1983) 955–963.
[2] S.A. Ahmed, D.P. Giddens, Pulsatile poststentotic flow studies with laser Doppler anemometry, J. Biomech. 17 (1984) 695–705.
[3] L.B. Goldstein, G.P. Samsa, D.B. Matchar, E.Z. Oddone, Multicenter review of preoperative risk factors for endarterectomy for asymptomatic carotid artery stenosis, Stroke 29 (1998) 750–753, https://doi.org/10.1161/01.STR.29.4.750.
[4] A.S. Jahromi, C.M. Clase, R. Maggisano, R. Bailey, H.A. Safar, C.S. Cinà, Progression of internal carotid artery stenosis in patients with peripheral arterial occlusive disease, J. Vasc. Surg. 50 (2009) 292–298, https://doi.org/10.1016/j.jvs.2009.02.236.
[5] G. Theodorou, D. Bellet, Laminar flows of a non-Newtonian fluid in mild stenosis, Comput. Methods Appl. Mech. Eng. 54 (1986) 111–123.
[6] V.L. Rayz, S.A. Berger, D. Saloner, Transitional flows in arterial fluid dynamics, Comput. Methods Appl. Mech. Eng. 196 (2007) 3043–3048, https://doi.org/10.1016/j.cma.2006.10.014.
[7] C. Methods, A. Mech, S. Morganti, F. Auricchio, D.J. Benson, F.I. Gambarin, S. Hartmann, T.J.R. Hughes, A. Reali, Patient-specific isogeometric structural analysis of aortic valve closure, Comput, Methods Appl. Mech. Energy 284 (2015) 508–520, https://doi.org/10.1016/j.cma.2014.10.010.
[8] D. Bluestein, C. Gutierrez, M. Londono, R.T. Schoephoerster, Vortex shedding in steady flow through a model of an arterial stenosis and its relevance to mural platelet deposition, Ann. Biomed. Eng. 27 (1999) 763–773, https://doi.org/10.

1114/1.230.
[9] B.K. Bharadvaj, R.F. Mabon, D.P. Giddens, Steady flow in a model of the human carotid bifurcation. Part I – flow visualization, J. Biomech. 15 (1982) 349–362.
[10] B.K. Bharadvaj, R.F. Mabon, D.P. Giddens, Steady flow in a model of the human carotid bifurcation. Part II-laser-Doppler anemometer measurements, J. Biomech. 15 (1982) 363–378.
[11] K. Perktold, M. Resch, G. Lang, Pulsatile non-Newtonian blood flow in three- dimensional carotid bifurcation models: a numerical study of flow phenomena under different bifurcation angles, J. Biomed. Eng. 13 (1991) 507–515.
[12] F.J.H. Gijsen, F.N. Van De Vosse, J.D. Janssen, The influence of the non-Newtonian properties of blood on the flow in large arteries: steady flow in a carotid bifurcation model, J. Biomech. 32 (1999) 601–608.
[13] A. Kashefi, M.M.B. Firoozabadi, M.A.G. Ahmadi, Multidimensional modeling of the stenosed carotid artery: a novel CAD approach accompanied by an extensive lumped model, Acta Mech. Sin. 30 (2014) 259–273.
[14] A. Sarrami-foroushani, M.N. Esfahany, A.N. Moghaddam, S. Rad, K. Firouznia, M. Shakiba, H. Ghanaati, I. David, A.F. Frangi, Velocity measurement in carotid artery: quantitative comparison of time-resolved 3D phase-contrast MRI and image-based computational fluid dynamics, Iran. J. Radiol. 12 (2015) 1–7, https://doi.org/10.5812/iranjradiol.18286.
[15] X. Huang, C. Yang, C. Yuan, F. Liu, G. Canton, J. Zheng, K. Woodard, G.A. Sicard, D. Tang, Patient-specific artery shrinkage and 3D zero-stress state in multi-component 3D FSI models for carotid atherosclerotic plaques based on in-vivo MRI data, Mol. Cell. Biomech. 6 (2009) 121–134.
[16] J.S. Stroud, S.A. Berger, D. Saloner, Numerical analysis of flow through a severely stenotic carotid artery bifurcation, J. Biomech. Eng. 124 (2002) 9–20.
[17] B.D. MacNeill, H.C. Lowe, M. Takano, V. Fuster, I.K. Jang, Intravascular modalities for detection of vulnerable plaque: current status, Arterioscler. Thromb. Vasc. Biol. 23 (2003) 1333–1342, https://doi.org/10.1161/01.ATV.0000080948.08888.BF.
[18] O. Ley, T. Kim, Determination of atherosclerotic plaque temperature in large arteries, Int. J. Therm. Sci. 47 (2008) 147–156, https://doi.org/10.1016/j.ijthermalsci.2007.01.034.
[19] W. Casscells, B. Hathorn, M. David, T. Krabach, W.K. Vaughn, H.A. McAllister, G. Bearman, J.T. Willerson, Thermal detection of cellular infiltrates in living atherosclerotic plaques: possible implications for plaque rupture and thrombosis, Lancet 347 (1996) 1447–1449, https://doi.org/10.1016/S0140-6736(96)91684-0.
[20] M. Naghavi, M. Madjid, K. Gul, M.S. Siadaty, S. Litovsky, J.T. Willerson, S.W. Casscells, Thermography basket catheter: in vivo measurement of the temperature of atherosclerotic plaques for detection of vulnerable plaques, Catheter. Cardiovasc. Interv. 59 (2003) 52–59, https://doi.org/10.1002/ccd.10486.
[21] K. Toutouzas, G. Benetos, M. Drakopoulou, P. Bounas, D. Tsekoura, K. Stathogiannis, I. Koutagiar, C. Aggeli, A. Karanasos, D. Panagiotakos, E. Siores, C. Stefanadis, Insights from a thermography-based method suggesting higher carotid inflammation in patients with diabetes mellitus and coronary artery disease, Diabetes Metab. 40 (2014) 431–438, https://doi.org/10.1016/j.diabet.2014.05.005.
[22] B.Y.J.M. Marshall, Physiological reactions of the human body to varying environmental temperatures, Am. J. Physiol. 120 (1937) 1–22.
[23] M.L. Ong, E.Y.K. Ng, A global bioheat model with self-tuning optimal regulation of body temperature using Hebbian feedback covariance learning, Med. Phys. 32 (2005) 3819–3831, https://doi.org/10.1118/1.2133720.
[24] A. Saxena, E.Y.K. Ng, V. Raman, Thermographic venous blood flow characterization with external cooling stimulation, Infrared Phys. Technol. 90 (2018) 8–19, https://doi.org/10.1016/j.infrared.2018.02.001.
[25] A. Saxena, V. Raman, E.Y.K. Ng, Study on methods to extract high contrast image in active dynamic thermography, Quant. InfraRed Thermogr. J. 6733 (2019) 1–17, https://doi.org/10.1080/17686733.2019.1586376.
[26] A. Saxena, V. Raman, E.Y.K. Ng, Single image reconstruction in active dynamic thermography: a novel approach, Infrared Phys. Technol. 93 (2018) 53–58, https://doi.org/10.1016/j.infrared.2018.07.020.
[27] L. Zhu, Theoretical evaluation of contributions of heat conduction and countercurrent heat exchange in selective brain cooling in humans, Ann. Biomed. Eng. 28 (2000) 269–277.
[28] B.H. Dennis, R.C. Eberhart, G.S. Dulikravich, U.T.A. Box, S.W. Radons, Finite-element simulation of cooling of realistic 3-D human head and neck, J. Biomech. Eng. 125 (2017) 832–840, https://doi.org/10.1115/1.1634991.
[29] A. Saxena, E.Y.K. Ng, S.T. Lim, Imaging modalities to diagnose carotid artery stenosis: progress and prospect, Biomed. Eng. Online 18 (2019) 1–23, https://doi.org/10.1186/s12938-019-0685-7.
[30] T.D. Capistrant, R.J. Gumnit, Detecting carotid occlusive disease by thermography, Stroke 4 (1973) 57–64.
[31] P.B. Morgan, J.V. Smyth, A.B. Tullo, N. Efron, Ocular temperature in carotid artery stenosis, Optom. Vis. Sci. 76 (1999) 850–854.
[32] B. Hofferberth, M. Gottschaldt, S. Dykan, Comparison of Doppler sonography and plate thermography for detection of carotid artery stenosis, Stroke 11 (1980) 27–30, https://doi.org/10.1161/01.STR.11.1.27.
[33] S.S. Varghese, S.H. Frankel, Numerical modeling of pulsatile turbulent flow in stenotic vessels, J. Biomech. Eng. 125 (2003) 445–460, https://doi.org/10.1115/1.1589774.
[34] Y. Yang, J. Liu, Detection of atherosclerosis through mapping skin temperature variation caused by carotid atherosclerosis plaques, J. Therm. Sci. Eng. Appl. 3 (2018) 1–9, https://doi.org/10.1115/1.4004109.
[35] J. Breeze, A. West, J. Clasper, Anthropometric assessment of cervical neurovascular structures using CTA to determine zone-speci fi c vulnerability to penetrating fragmentation injuries, Clin. Radiol. 68 (2013) 34–38, https://doi.org/10.1016/j.crad.2012.05.011.
[36] M. Bommadevara, L. Zhu, Temperature difference between the body core and arterial blood supplied to the brain during hyperthermia or hypothermia in humans, Biomechanics Model. Mechanobiol. 1 (2002) 137–149, https://doi.org/10.1007/s10237-002-0011-2.
[37] C.R. Ethier, C.A. Simmons, Introductory Biomechanics: from Cells to Organisms, (2007).
[38] O. Ley, T. Kim, Calculation of arterial wall temperature in atherosclerotic arteries: effect of pulsatile flow, arterial geometry, and plaque structure, Biomed. Eng. Online 18 (2007) 1–18, https://doi.org/10.1186/1475-925X-6-8.
[39] C.M. Crowder, R. Tempelhoff, M.A. Theard, M.A. Cheng, A. Todorov, R.G. Dacey, Jugular bulb temperature: comparison with brain surface and core temperatures in neurosurgical patients during mild hypothermia, J. Neurosurg. 85 (1996) 98–103, https://doi.org/10.3171/jns.1996.85.1.0098.
[40] H.H. Penne, Analysis of tissue and arterial blood temperature in the resting human forearm, J. Appl. Phisiol. 1 (1948) 93–122.
[41] Z.S. Deng, J. Liu, Mathematical modeling of temperature mapping over skin surface and its implementation in thermal disease diagnostics, Comput. Biol. Med. 34 (2004) 495–521, https://doi.org/10.1016/S0010-4825(03)00086-6.
[42] Z.Y. Li, F.P.P. Tan, G. Soloperto, N.B. Wood, X.Y. Xu, J.H. Gillard, Flow pattern analysis in a highly stenotic patient-specific carotid bifurcation model using a turbulence model, Comput. Methods Biomech. Biomed. Eng. 18 (2015) 1099–1107, https://doi.org/10.1080/10255842.2013.873033.
[43] P.A. Dharmasaroja, N. Uransilp, A. Watcharakorn, P. Piyabhan, Accuracy of carotid duplex criteria in diagnosis of significant carotid stenosis in Asian patients, J. Stroke Cerebrovasc. Dis. 27 (2018) 778–782, https://doi.org/10.1016/j.jstrokecerebrovasdis.2017.10.014.
[44] S. Patankar, Numerical Heat Transfer and Fluid Flow, (1980), https://doi.org/10.1016/j.watres.2009.11.010.
[45] A. Saxena, E.Y.K. Ng, Steady and pulsating flow past a heated rectangular cylinder (s) in a channel, J. Thermophys. Heat Transf. 8722 (2017) 1–13, https://doi.org/10.2514/1.T5265.
[46] K. Supradeepan, A. Roy, Characterisation and analysis of flow over two side by side cylinders for different gaps at low Reynolds number: a numerical approach, Phys. Fluids 26 (2014) 1–29, https://doi.org/10.1063/1.4883484.
[47] D. Arumuga Perumal, G.V.S. Kumar, A.K. Dass, Lattice Boltzmann simulation of flow over a circular cylinder at moderate Reynolds numbers, Therm. Sci. 18 (2014) 1235–1246, https://doi.org/10.2298/TSCI110908093A.
[48] P. Hung, K. Lee, L. Tsai, Contact-free heart rate measurement using multiple video data, AIP Conf. Proc. 2013, pp. 57–66, , https://doi.org/10.1063/1.4824996.
[49] N. Sun, M. Garbey, A. Merla, I. Pavlidis, Imaging the cardiovascular pulse, Proc IEEE Comput. Soc. Conf. Comput. Vis. Pattern Recognit. 2 (2005) 416–421, https://doi.org/10.1109/CVPR.2005.184.
[50] S.Y. Chekmenev, A.A. Farag, W.M. Miller, E.A. Essock, A. Bhatnagar, Multiresolution approach for noncontact measurements of arterial pulse using thermal imaging BT - augmented vision perception in infrared: algorithms and applied systems, 2006 Conf. Comput. Vis. Pattern Recognit. Work., New York, USA, 2009, pp. 87–112, , https://doi.org/10.1007/978-1-84800-277-7_4.
[51] M. Yang, Q. Liu, T. Turner, Y. Wu, Vital sign estimation from passive thermal video, 26th IEEE Conf. Comput. Vis. Pattern Recognition, CVPR, 2008, , https://doi.org/10.1109/CVPR.2008.4587826.
[52] F. Xu, T.J. Lu, K.A. Seffen, E.Y.K. Ng, Mathematical modeling of skin bioheat transfer, Appl. Mech. Rev. 62 (2009) 1–35, https://doi.org/10.1115/1.3124646.
[53] FLIR, FLIR T1020, Prod. Datasheet, (2015), pp. 1–2 https://www.transcat.com/flir-t1020-12-72501-0101-252179 , Accessed date: 14 May 2019.
[54] A. Bit, D. Ghagare, A.A. Rizvanov, H. Chattopadhyay, Assessment of influences of stenoses in right carotid artery on left carotid artery using wall stress marker, BioMed Res. Int. (2017) (2017) 1–13, https://doi.org/10.1155/2017/2935195.
[55] G. Rappitsch, K. Perktold, Pulsatile albumin transport in large arteries: a numerical simulation study, J. Biomech. Eng. 118 (2008) 511, https://doi.org/10.1115/1.2796038.
[56] Y. Yang, J. Liu, Detection of atherosclerosis through mapping skin temperature variation caused by carotid atherosclerosis plaques, J. Therm. Sci. Eng. Appl. 3 (2011) 031005, , https://doi.org/10.1115/1.4004109.
[57] A. Bit, H. Chattopadhyay, Assessment of rheological models for prediction of transport phenomena in stenosed artery, Prog. Comput. Fluid Dyn. An Int. J. 14 (2014) 363, https://doi.org/10.1504/pcfd.2014.065468.
[58] A. Razavi, E. Shirani, M.R. Sadeghi, Numerical simulation of blood pulsatile flow in a stenosed carotid artery using different rheological models, J. Biomech. 44 (2011) 2021–2030, https://doi.org/10.1016/j.jbiomech.2011.04.023.
[59] A. Bit, H. Chattopadhyay, Numerical investigations of pulsatile flow in stenosed artery, Acta Bioeng. Biomech. 16 (2014), https://doi.org/10.5277/ABB-00029-2014-05.